Tunable carbon surface from mono- to multi-metallic single atoms

Wei-Hong Lai,[1,2,3] Heng Wang,[4] Quan Jiang,[5,8] Zi-Chao Yan,[3] Han-Wen Liu,[3] Yao-Jie Lei,[3] Lingfei Zhao,[3] Wang zhang,[1] Lei Wang,[1]* Hirofumi Yoshikawa,[5] Daiju Matsumura,[6] Yun-Xiao Wang,[3]* Qiao Sun,[7] Jia-Zhao Wang,[3] Hua-Kun Liu,[3] Shu-Lei Chou,[3]* Shi-Xue Dou[3]

[1] College of Materials Science and Engineering, Shenzhen University, Shenzhen 518060, China.

[2] College of Physics and Optoelectronic Engineering, Shenzhen University, Shenzhen 518060, China.

[3] Institute for Superconducting & Electronic Materials, University of Wollongong, Innovation Campus, Wollongong, NSW 2500, Australia.

[4] School of Material and Chemical Engineering, Zhengzhou University of Light Industry, Zhengzhou 450002, China.

[5] State Key Laboratory of Radiation Medicine and Protection, Collaborative Innovation Centre of Radiation Medicine of Jiangsu Higher Education Institutions, School for Radiological and Interdisciplinary Sciences, Soochow University, Suzhou 215123, China.

[6] School of Science and Technology, Kwansei Gakuin University, 2-1 Gakuen, Sanda, Hyogo 669-1337, Japan.

[7] Quantum Beam Science Center, Japan Atomic Energy Agency, Sayo-gun, Hyogo 679-5148, Japan.

[8] Key Laboratory for Ultrafine Materials of Ministry of Education, Shanghai Key Laboratory of Advanced Polymeric Materials, School of Materials Science and Engineering, East China University of Science and Technology, Shanghai 200237, China.

Abstract: The control of carbon surface requires a highly compositional complexity at atomic scale, which is vital but challenging. Herein, we develop a general strategy to co-doping up to seven species of metallic single atoms into nitrogen-doped carbon (NC), leading to multi-single-atom doped carbon (MSAC), denoted as MSAC-7 ($(PtFeIrRuCoPdIn)_1$@NC). Significantly, we can flexibly tune the complexity of carbon surface, including senary (MSAC-6, $(PtFeIrRuCoPd)_1$@NC), quinary (MSAC-5, $(PtFeIrRuCo)_1$@NC), quaternary (MSAC-4, $(PtFeIrRu)_1$@NC), ternary (MSAC-3, $(PtFeIr)_1$@NC), and binary (MSAC-2, $(PtFe)_1$@NC) structures. The MSAC demonstrates an unexpected catalytic performance towards oxygen reduction reactions (ORR) and hydrogen evolution reactions (HER), that is, the mass activity of ORR of noble metals of MSAC-6 shows 164 times higher than Pt/C and MSAC-4 has a comparable HER performance with Pt/C. Significantly, the electrocatalytic behaviors of MSAC have been theorectically and experimentally revealed. This work confirms that MSAC can be an efficient catalysts by tuning the complexity of carbon surface due to the synergistic effects amongst single atoms. The developed non-selective charge compensation method as a versatile tool builds a library of multi-metallic single-atom catalysts (SACs), giving a new insight into primary surface science and extending the realm of SACs.

Heterogeneous surfaces are of intrinsic importance for catalysis, which provides active sites and the natural environment to accelerate a wide range of reactions.[1] Heteroatom-doped carbon materials represent as a unique class of effective catalysts, which can induce disorder and defects and change the electronic structure of the carbon matrix due to the difference of atomic radius, bond length and electronegativity.[2] For instance, nitrogen-doping can lead to positive charge on carbon, and the neighbouring carbon can serve as active sites. N dopant is essential for carbon matrix due to its electron accepting ability and superior electrochemical stability.[3] Boron and phosphorus possess lower electronegativity than that of carbon, thus the doped B or P dopants would become inferior active sites.[4] Metallic single-atom doping, on the other hand, thrives on maximal atomic utilization as well as distinct electronic and geometric structures.[1, 5-6] Correspondingly, various single-atom catalysts have been fabricated and proven to deliver unexpected catalytic performance in a wide scope of reactions, such as hydrogenation reactions,[7-9] hydrogen evolution reactions,[10-11] oxygen reduction reactions,[12 13] oxygen evolution reactions (OER),[13] CO oxidation reactions,[8, 14] CO_2 reduction reactions,[15] NO oxidation reactions,[11] N_2 reduction reactions (NRR),[16] electrochemical reactions in batteries,[17-19] and other reactions.[20-23] Mono single-atom metals can be anchored on carbon backbones via defect engineering,[24] atomic layer deposition,[25]and coordinating with organic ligands.[12]

Notably, Beller et al. have illuminated the direction on bi- and multimetallic SACs for the next years, but it is extremely challenging to co-disperse different metallic elements in isolation on a support. Two reports are initiated to explore the feasibility of bi-metallic SACs, including Pt_1-Sn_1, as well as Fe/Co, Ru/Fe, Ru/Co, and Ru/Ni, respectively.[26 27] Also, a defected C/N graphene surface modified with atomic Pt-Co suggested high ORR activity via synergistic interactions between atomic Pt-Co pair and the neighboring non-metal atoms.[28] It is noticeable that the atomic interaction amongst the adjacent atoms in a certain local environment can significantly tailor the electronic structure of the metal atoms and alter charge distribution to form atomic Co-Pt-N-C coordination structures as active sites, thereby enhancing ORR performance. Thus, increasing atomic metal species on carbon support is vital to tune the structural disorder of carbon surface, which, in turn, affects the electronic structures and physical properties of carbon skeletons, leading to a new generation of high-activity SACs for a large variety of applications, especially for domino and tandem reactions in the future. The successful preparation of high compositional single-atom doped carbon is also highly significant to the synthetic chemistry and life-science as well as to explore the limitation of metal-doped carbon materials.

Herein, we develop a non-selective charge compensation strategy to prepare multi-single-atom doped carbon (MSAC) in which a sodium p-toluenesulfonate (PTS-Na) doped polypyrrole (S-PPy) polymer is designed to anchor discretionary mixtures of multiple metal cations, including iron (Fe^{3+}), cobalt (Co^{3+}), ruthenium (Ru^{3+}), palladium (Pd^{2+}), indium (In^{3+}), iridium (Ir^{2+}), and platinum (Pt^{2+}) . As illustrated in Figure 1, the carbon surface can be tuned with different level of compositional complexities, including unary Pt_1@NC, binary (MSAC-2, $(PtFe)_1$@NC), ternary (MSAC-3, $(PtFeIr)_1$@NC), quaternary (MSAC-4, $(PtFeIrRu)_1$@NC), quinary (MSAC-5, $(PtFeIrRuCo)_1$@NC), senary (MSAC-6, $(PtFeIrRuCoPd)_1$@NC), and septenary (MSAC-7, $(PtFeIrRuCoPdIn)_1$@NC) samples. The structural evolution of carbon surface dictates the activities of both ORR and HER. The senary MSAC-6 achieves the ORR mass activity of 18.1 $A \cdot mg_{metal}^{-1}$ at 0.9 V (Vs reversible hydrogen electrode (RHE)) over 30K cycles, which is 164 times higher than that of commercial Pt/C. The quaternary MSAC-4 presented a comparable HER catalytic capability with that of Pt/C. These results indicate that the highly complexed carbon surface can enhance its ability over general electrochemical catalytic reactions. The mechanisms

regarding of the ORR and HER activities of the alternated carbon surface are also theoretically and experimentally investigated in this work, showing that the synergistic effects amongst the co-doped atoms can activate or inactivate certain single-atom sites.

Results

Structural characterization

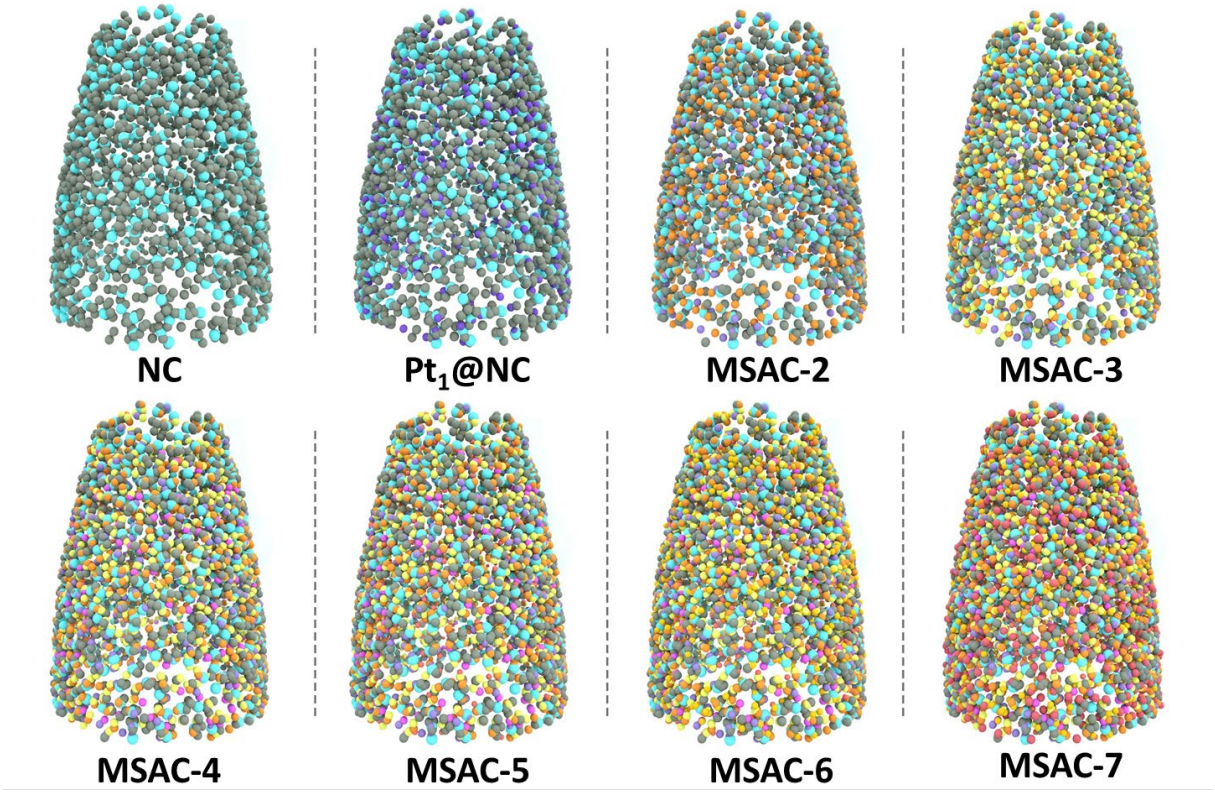

Figure 1. The illustration of structure of MSAC

It is known that the different metal cations can easily aggregate together to form particles due to the different redox potential especially under a high-temperature sintering. Stabilizing metal cations with strong bonding, thus, is vital for the synthesis of multi-single-atom doped carbon. In this work, PTS-Na is utilized as the functionalized counterion, interacting with metal cations (Figure S1). The sodium ions on PTS-Na migrate off the oxidized S-PPy during the polymerization process and are compensated via metal ions (S-PPy-M^{x+}), resulting in a stabilized bond during the sintering process. After high-temperature sintering, the precursors of S-PPy stabilized metal cations can be converted into single atom metals implanted onto nitrogen doped carbon fibres with tailored surface. In particular, the precursors of metal cations can be controlled to contain various compositional species from elements of Pt, Fe, Ir, Ru, Co, Pd, and In. As shown in Figure 1, different combinations of cations, including Pt^{2+}, Pt^{2+}/Fe^{3+}, $Pt^{2+}/Fe^{3+}/Ir^{2+}$, $Pt^{2+}/Fe^{3+}/Ir^{2+}/Ru^{3+}$, $Pt^{2+}/Fe^{3+}/Ir^{2+}/Ru^{3+}/Co^{3+}$, $Pt^{2+}/Fe^{3+}/Ir^{2+}/Ru^{3+}/Co^{3+}/Pd^{2+}$, and $Pt^{2+}/Fe^{3+}/Ir^{2+}/Ru^{3+}/Co^{3+}/Pd^{2+}/In^{3+}$, are selected to prepare the controllable surface, leading to the formation of Pt_1@NC, binary (MSAC-2, $(PtFe)_1$@NC), ternary (MSAC-3, $(PtFeIr)_1$@NC), quaternary (MSAC-4, $(PtFeIrRu)_1$@NC), quinary (MSAC-5, $(PtFeIrRuCo)_1$@NC), senary (MSAC-6, $(PtFeIrRuCoPd)_1$@NC), and septenary (MSAC-7, $(PtFeIrRuCoPdIn)_1$@NC) samples, respectively. In contrast, Pt particles are

formed on carbon framework when PTS-Na is not added on PPy surface as functional groups (Figure S2), indicating that the PTS-Na plays a vital role in maintaining the single-atom status of various metals.

As shown in Figure 2AI, the high angle annular dark field (HAADF)-scanning transmission electron microscopy (STEM) image at high resolution verifies that a variety of the bright-contrast single atoms are uniformly dispersed on carbon matrix surface of MSAC-7 without agglomeration during the high-temperature annealing. The STEM-energy dispersive spectroscopy (EDS) elemental maps further confirm that the involved elements (M = Pt, Ir, Pd, Ru, In, Co, Fe) are uniformly distributed over the entire architecture (Figure 2AII-VIII, Figure S3). The overlapped elemental signals on the corresponded architecture demonstrate a two-dimensional colourful scattergram (Figure 2AIX), indicating a compositional high-complexity carbon surface.

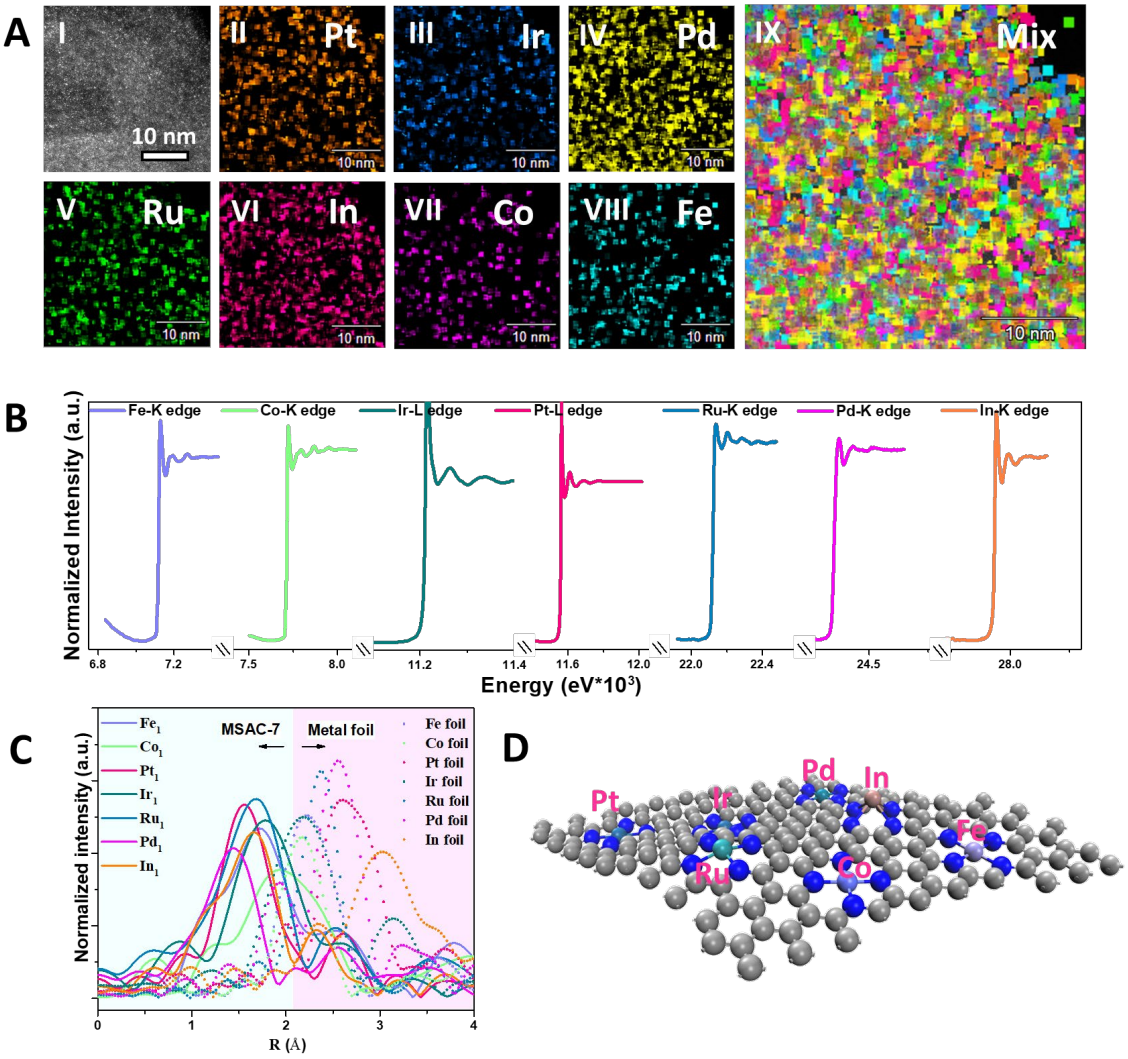

Figure 2. The surface structure of MSAC-7. (A) The HAADF image (I) and the corresponding elemental maps of Pt, Ir, Pd, Ru, In, Co, Fe of MSAC-7 (II-IX). (B) The XAS spectra across different energy regions of dissimilar elements in MSAC-7. (C) The FT- EXAFS spectra of the composed elements on MSAC-7 and their corresponding foils. (D) The illustration of the fitted structure of MSAC-7. The black ball represents carbon, the blue ball represents nitrogen.

To explore the local order information of metal atoms of MSAC, the X-ray adsorption spectroscopy (XAS) was conducted due to its atomic selectivity and high sensitivity [29-30]. The both parts of X-ray absorption near edge structure (XANES) and X-ray absorption fine structure (EXAFS) of the obtained XAS have been demonstrated in Figure 2B, which shows the specific energy regions across a range of metal atoms in MSAC-7, including Fe-K edge, Co-K edge, Ir-L edge, Pt-L edge, Ru-K edge, Pd-K edge, and In-K edge. In principle, the successful detection of these metal atoms confirms the multi-metallic carbon surface, which is consistent with the EDS results. Also, the Fourier transform (FT)-EXAFS spectra of MSAC-7 and the referenced metal foil were employed to analyse their coordination environment. As shown in Figure 2C, R-space of all metal atoms of MSAC-7, including Fe_1, Co_1, Ir_1, Pt_1, Ru_1, Pd_1, and In_1, shows a blue shift to a low-coordination bonding distance, and in turn, their corresponding foils show their characteristic metal-metal distance in a high-coordination region. These results indicate that the metal atoms in MSAC-7 are isolated as single-atom dopants instead of metal phase. Additionally, the EXAFS fitting of R-space was performed for simulating their coordinated structure of each single atom of MSAC-7. Their simulated model of local structure suggests the different atoms form a similar tetradentate structures (Pt_1-4N, Fe_1-4N, Pd_1-4N, Ir_1-4N, Ru-4N, Co-4N, and In_1-4N) (Figure S4, Table S1). The carbon surface of MSAC-7 is supposed to consist of these individual single-atom complex as shown in Figure 2D. The loading mass of metal elements on MSAC-7 was confirmed by inductively coupled plasma-optical emission spectrometry (ICP-AES) (Table S2).

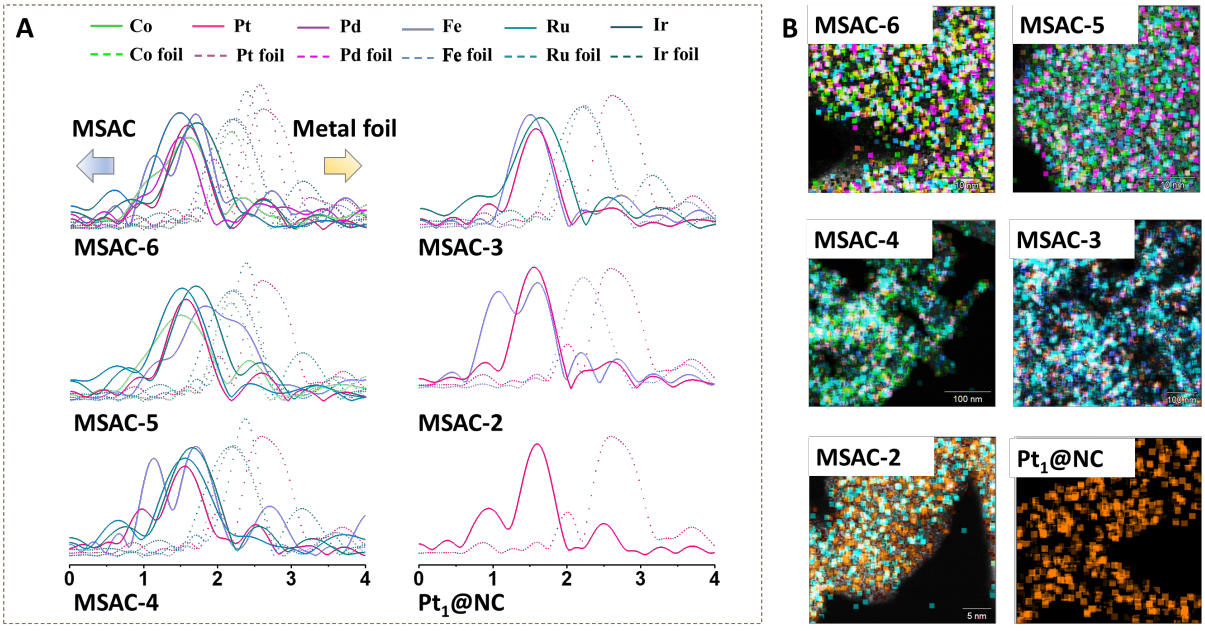

Figure 3. The tune of multi-single-atom structure of carbon surface. (A) The FT-EXAFS spectra and STEM elemental maps (inset images) of the composed elements of MSAC-6, MSAC-5, MSAC-4, MSAC-3, MSAC-2, and Pt_1@NC, showing FT- EXAFS spectra of their referenced metal foils as well. (B) The mixed STEM-EDS elemental maps of MSAC-6, MSAC-5, MSAC-4, MSAC-3, MSAC-2, and Pt_1@NC.

Also, we demonstrated the versatility in preparing a series of carbon surface from high complexity to low complexity: MSAC-6, MSAC-5, MSAC-4, MSAC-3, MSAC-2, and unary Pt_1@NC. Similar to multimetallic single atoms in MSAC-7, the metal atoms in MSAC-6, MSAC-5, MSAC-4, MSAC-3, MSAC-2, and Pt_1@NC are anchored on carbon surface as isolated single

atoms, showing a number of high-contrast bright spots (Figure S5). The involved elements are uniformly distributed across their respective architectures (Figure S6-12). The composed elements of MSAC-6, MSAC-5, MSAC-4, MSAC-3, MSAC-2, and Pt_1@NC were also confirmed by XAS spectra (Figure S13). Additionally, the EXAFS spectra of MSAC-6, MSAC-5, MSAC-4, MSAC-3, MSAC-2, and Pt_1@NC (Figure 3A) show similar low coordination shell without metal-metal characteristic peaks, which confirm their isolated local structures. The success in tuning the diversity of single-atom metal dopants indicates the proposed method enable to precisely control the single-atom dopants of the carbon surface as well as the polybasic compositions. The mixed EDS elemental mappings as shown in Figure 3B visually present that a variety of elements can be evenly distributed on carbon surface without agglomeration. This result also indicates that all metal species can be tuned in a descending order from senary to unary. Furthermore, the X-ray diffraction (XRD) patterns of all MSAC samples are well consistent with the carbon. There are no metal phases formed in any MSAC samples, further implying that the loaded metals are very likely to be atomically dispersed on the support without agglomeration (Figure S14). For comparison, a series of unary single-atom catalysts, including Ir_1@NC, Ru_1@NC, Co_1@NC, Fe_1@NC, In_1@NC, and Pd_1@NC were also prepared (Figure S15).

Electrochemical characterization

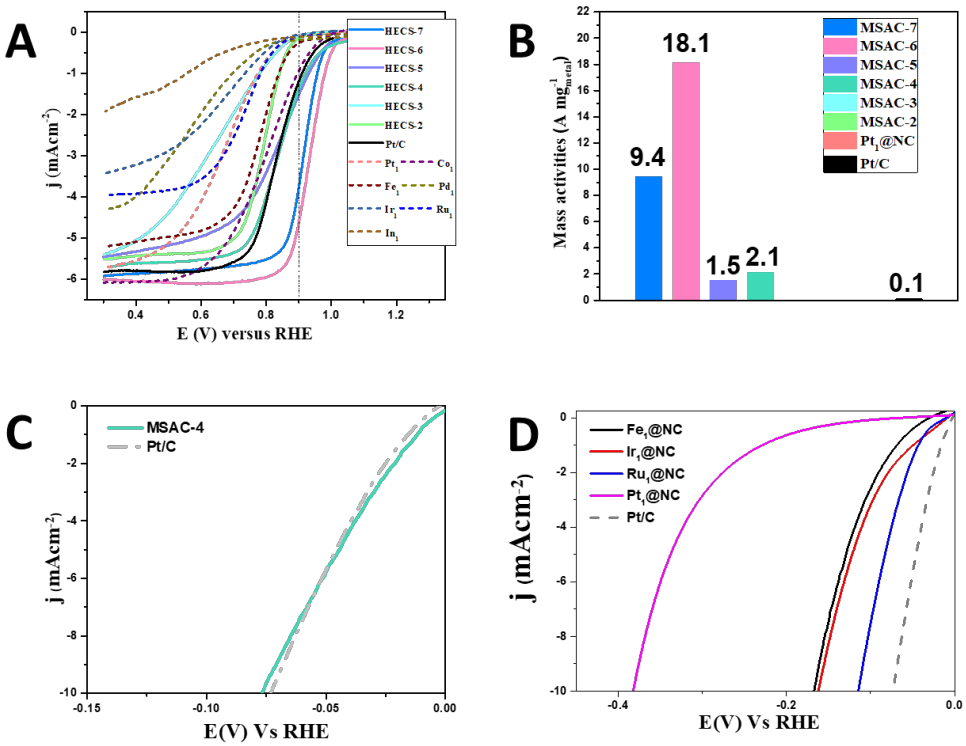

Figure 4. ORR and HER performance. (A) ORR polarization curves for MSAC-7, MSAC-6, MSAC-5, MSAC-4, MSAC-3, MSAC-2, Pt_1@NC, Ir_1@NC, Ru_1@NC, Co_1@NC, Fe_1@NC, Pd_1@NC, In_1@NC, and Pt/C (B) The ORR mass activity of MSAC-7, MSAC-6, MSAC-5, MSAC-4, MSAC-3, MSAC-2, Pt_1@NC, and Pt/C. (C) Polarization curves of the HER of samples: MSAC-4 and commercial Pt/C. (D) Polarization curves of the HER of samples: Pt_1@NC, Ir_1@NC, Ru_1@NC, Fe_1@NC and commercial Pt/C.

Compared with the pristine carbon surface, the physical properties of MSAC are changed due to the multi-composition-induced disordered properties. As a proof of our concept, these as-prepared MSAC samples were utilized to comprehensively investigate their catalytic activities on ORR and HER, respectively. Figure 4A shows the ORR polarization curves of different catalysts recorded at room temperature at a sweep rate of 10 mV s^{-1} with a rotation rate of 1600 rpm in O_2-saturated 0.1 M KOH solution. For a clear comparison, the unary single atom materials, including Pt_1@NC, Fe_1@NC, Ir_1@NC, Ru_1@NC, Co_1@NC, Pd_1@NC, and In_1@NC, have been prepared. It is evident that the MSAC-6 has the highest half-wave potential ($E_{1/2}$ = 0.93 V), compared with the individual single-atom counterparts, including Pt_1@NC, Fe_1@NC, Ir_1@NC, Ru_1@NC, Co_1@NC, and Pd_1@NC. The result indicates that the regulation of multiple elements of MSAC would synergistically improve ORR performance. Additionally, the mass activity of MSAC-6 can be calculated to be 18.1 $A \cdot mg_{metal}^{-1}$ at 0.9 V (Vs reversible hydrogen electrode (RHE)), which is 164 times higher than commercial Pt/C (0.11 $A \cdot mg_{Pt}^{-1}$) (Figure 4B). The number of electrons transferred (n) is estimated to be ~3.8 at 0.3-0.6 V from the slopes of the Koutecky-Levich plots, indicating the nearly complete reduction of O_2 (Figure S16). To the best of our knowledge, the MSAC-6 achieved the highest ORR mass activity in alkaline solution under comparable conditions, including various PMG-based nanomaterials (Table S3). An accelerated durability test between 0.6 and 1.0 V shows that there is no obvious shift at 0.9 V after 30000 cycles (Figure S17). Notably, the mass activity at 0.9 V increases in the sequence: Pt_1@NC = MSAC-2 = MSAC-3 < Pt/C < MSAC-5 < MSAC-4 < MSAC-7 < MSAC-6, indicating that the excellent ORR performance can be only achieved when the carbon matrix is controlled to high compositional single-atom dopants with exceeding four metallic elements. It is noticeable that the MSAC-7 also delivers an excellent ORR activity with a high half-wave potential ($E_{1/2}$ = 0.92 V) and a mass activity of 9.2 $A \cdot mg_{metal}^{-1}$ at 0.9 V, which is much better than those of Pt/C. These results indicate that carbon surface with high elemental complexity can present the enhanced ORR activity beyond that of any unary catalytic units of their corresponding elements. The alternative metal combination, however, would affect their ORR performance either. For instance, even though further doped with extra In_1, the MSAC-7 ($(PtFeIrRuCoPdIn)_1$@NC) shows inferior performance than MSAC-6 ($(PtFeIrRuCoPd)_1$@NC). Moreover, the diverse compositions of MSAC enable a wide potential application. As shown in Figure 4C, the MSAC-4 achieved a comparable HER performance with the commercial Pt/C in 1 M KOH solution. As shown in Figure 4D, however, the corresponding unary single-atom catalysts, including Pt_1@NC, Fe_1@NC, Ir_1@NC, and Ru_1@NC, indicate an inferior HER performance compared with Pt/C. There results further indicate that the multimetalllic carbon surface can enhance the catalytic capability and show highly potential applications as new multifunctional catalysts.

Discussion

Catalytic mechanism of MSAC for ORR

Generally, the ORR involves an indirect four-electron mechanism, of which the two-electron pathway converses to hydrogen peroxide, followed by further reduction to water[31]. As a consequence, the four-electron ORR has multiple intermediates, involving OOH*, O*, and OH*, which are strongly correlated. The binding energies of OOH*, O*, and OH* are expected to be moderate but not too strong or too week. For instance, the strong bond between homogeneous catalyst and oxygen limits the proton-electron transfer to O* or OH* and in turn, for materials that bind oxygen too weakly, the activity is limited by proton-electron transfer to O_2* or splitting of O-O bond. For multi-metallic carbon surface, thus, the compositional complexity of catalysts is

expected to gentle the adsorption energy of intermediates due to the synergistic effect amongst metals. Also, the atomic-level dispersion can probably overcome the kinetic challenges in diffusion of intermediates.

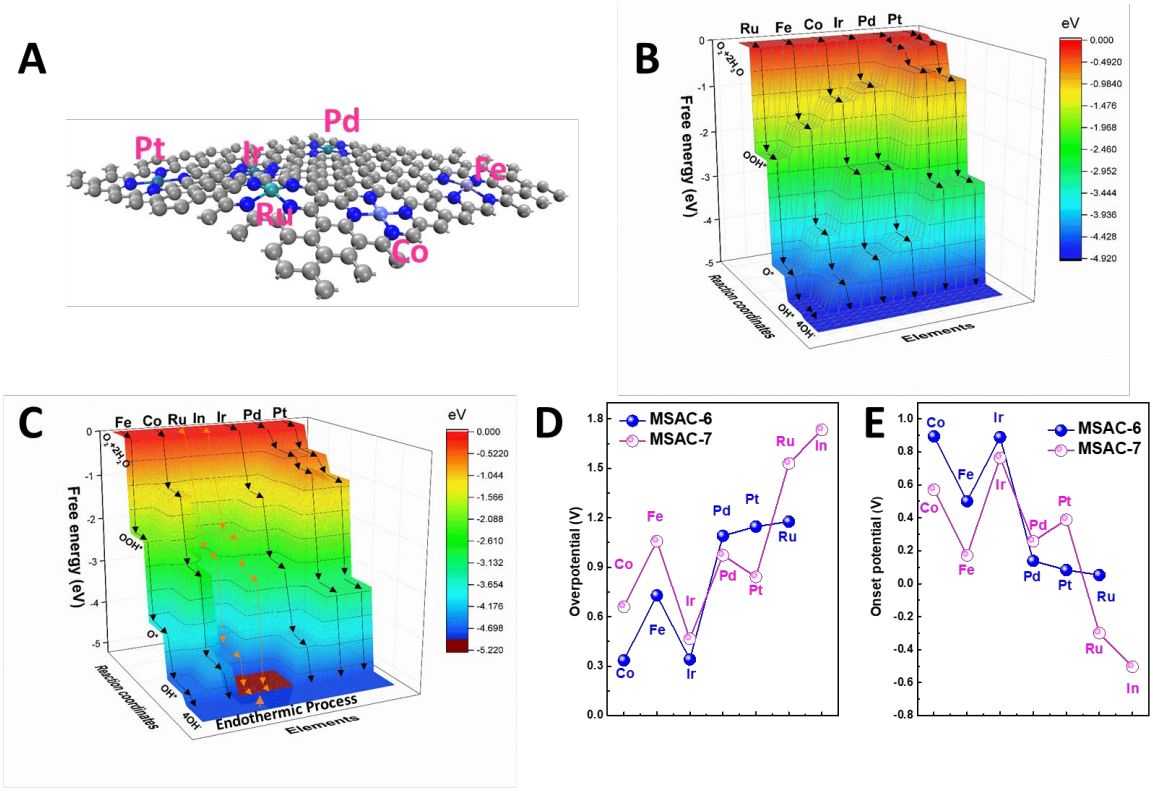

Figure 5. Theoretical calculation of MASC-6 and MSAC-7. (a) Structural illustration of MSAC-6. 3D theoretical free energy diagram for MSAC-6 (B) and MSAC-7 (C). (D) Overpotential of each single-atom unit on MSAC-6 and MSAC-7. (E) Onset potential of each single-atom unit on MSAC-6 and MSAC-7.

To investigate the synergistic effect, DFT calculations were performed on each different coordination structures of MSAC-6 and MSAC-7. The EXAFS fitting of R-space is performed for simulating their coordinated structure of each single atom of MSAC-6. As shown in Figure 5A, their simulated model of local structure suggests MSAC-6 shows a similar structure with MSAC-7 (Figure 2D). Tetradentate structures, including Pt_1-4N, Fe_1-4N, Pd_1-4N, Ir_1-4N, Ru-4N, and Co-4N, are mainly formed on MSAC -6 (Figure S18, Table S1). The optimized structures of MSAC-6 and MSAC-7 are utilized to build up the periodical surface models as it serves as the real host under ORR conditions (Figure S19 and S20). The corresponding Gibbs free energies (ΔG_i, i = OOH*, O*, and OH*) are calculated and provided (Figure S21 and S22). Although the local coordinated structure of MSCA-6 is highly similar to MSAC-7, it is noticeable that the combination of adjacent atoms could strongly affect the activity. For a better comparison, contour plot of 3D free energy profile can be constructed based on the calculated activities of different metal sites of MSAC-6 and MSAC-7. As shown in Figure 5B, all metal atoms on MSAC-6 show a totally exothermic process in each step, indicating their active surface for the overall $4e^-$ ORR. The ORR activities of MSAC-7, however, are decreased for the whole $4e^-$ ORR pathway by introducing the In_1 single atom into the structure. The pathways for the transition from *OH to OH^- of In_1 and Ru_1 are an endothermic process, indicating their inactive surface for the overall $4e^-$

ORR (Figure 5C). This result reveals that an appropriate combination of compositions is very important for the catalytic efficiency as the introduced new atom can possibly inactivate their neighbor atoms. In particular, the ORR 3D free energy profile of MSAC-6 shows a ladder-like configuration, which means the different single atoms can serve as a key role in the conversion of different intermediates. Accordingly, the overpotential of each single atom on MSAC-6 and MSAC-7 were summarized as shown in Figure 5D. The Co_1 of MSAC shows the most energetically favourable configuration on ORR with a low overpotential of 0.33 V. In contrast, the most active single atom Ir_1 of MSAC-7 only present an overpotential of 0.46 V. Also, the average overpotential of MSAC-6 is 0.8 V, which is better than that of MSAC-7 (1.04 V). Consequently, the onset potential of MSAC-6 is higher than that of MSAC-7, indicating the more active surface of MSAC-6 (Figure 5E). These theoretical results are consistent with the electrochemical-test results as shown in Figure 4.

Catalytic mechanism of MSAC for HER

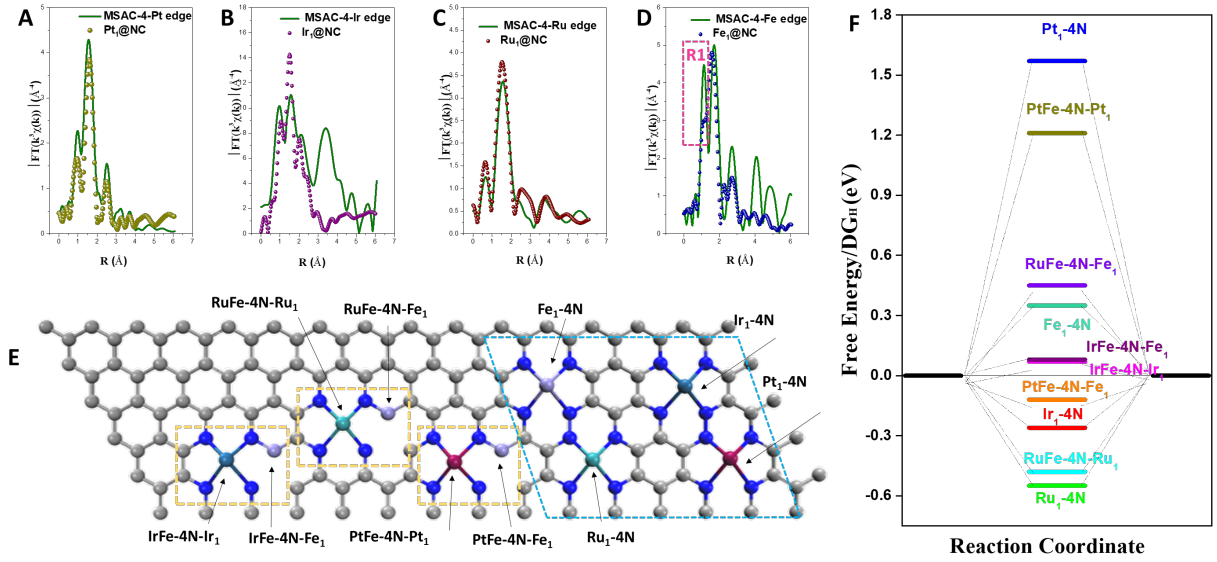

Figure 6. Structural characterization of MASC-4. (A-D) The K^3-weighted Fourier transform (FT) spectra from EXAFS of samples $(PtIrRuFe)_1$@NC and Pt_1@NC, Ir_1@NC, Ru_1@NC, Fe_1@NC on Pt edge (A), Ir edge (B), Ru edge (C), and Fe edge (D). (E) Two parts have been considered in fitting its structure of MSAC-4. The first part is Pt_1, Ir_1, Ru_1, and Fe_1 had independent local structures, which are Fe_1-4N, Pt_1-4N, Ir_1-4N, and Ru_1-4N (blue box). The other part we considered here is that the low-coordination has a high possibility to sit the side of precious metal groups (Pt/Ir/Ru), forming PtFe-4N-Pt_1, PtFe-4N-Fe_1, IrFe-4N-Ir_1, IrFe-4N-Fe_1, RuFe-4N-Ru_1 and RuFe-4N-Fe_1 (yellow box). (F) The free energy diagrams for the HER on Pt_1-4N, Ir_1-4N, Ru_1-4N, Fe_1-4N, PtFe-4N-Pt_1, IrFe-4N-Ir_1, RuFe-4N-Ru_1, PtFe-4N-Fe_1, IrFe-4N-Fe_1, RuFe-4N-Fe_1.

The optimal MASC-4 for HER was selected as an example to have detailed structural characterization and theoretical calculation. The previous reports have been experimentally and theoretically confirmed that the co-dopants of non-metal elements, such as boron, nitrogen, phosphorus, and sulphur, were able to increase the HER capability due to the synergistic effect between doped elements.[32] Our analysis also suggest that the co-doped single-atom metals can synergistically enhance the HER performance via favourable combination of elements. According

to the XAS results, the single atoms Pt_1, Ir_1 and Ru_1 on sample MSAC-4 are likely to have a similar atomic coordination with Pt_1@NC, Ir_1@NC, and Ru_1@NC due to the highly overlapped EXAFS spectra on the first shell as shown in Figure 6A-C. In contrast, the further doped Fe_1 single atoms on MSAC-4 have a strong low coordination peak, which is indicated by rectangle R1 (Figure 6D). These low coordinated Fe_1 structure suggests that Fe_1 can sit along with Pt_1, Ir_1, and Ru_1, leading to a strong correlation among these atoms, although parts of single Fe_1 single atoms also formed a same shell with Fe_1@NC. In order to confirm the synergistic effect between different metal atoms, the fitting of EXAFS spectra on MSAC-4 are performed. Based on the EXAFS spectra and our simulated structural models, the single atoms Pt_1, Ir_1 and Ru_1 on MSAC-4 are prone to form Pt_1-4N, Ir_1-4N and Ru_1-4N structures (Figure S23). In contrast, the doped Fe_1 single atoms on MSAC-4 have a strong low coordination peak and a high coordination peak, which is corresponding to Fe_1-4N and Fe_1-1N1C (Figure S24), respectively. These low coordinated Fe_1-1N1C is subject to sit along with Pt_1, Ir_1, and Ru_1, leading to strong interaction with these atoms as illuminated in Figure 6E. Also, the high resolution of FFTI-HAADF images of MSAC-4 show that the Fe atom (low contrast) has a high possibility to sit the side of precious metal groups (Pt/Ir/Ru) (high contrast), forming PtFe-4N, IrFe-4N, and RuFe-4N (Figure S25). The density functional theory (DFT) calculation also was used to confirm our hypothesis. Based on the fitting models of MSAC-4, the corresponding active units, including Fe_1-4N, Pt_1-4N, Ir_1-4N, Ru_1-4N, PtFe-4N-Pt_1, PtFe-4N-Fe_1, IrFe-4N-Ir_1, IrFe-4N-Fe_1, RuFe-4N-Ru_1 and RuFe-4N-Fe_1, were constructed (Figure S26). As shown in Figure 6F, the active sites of PtFe-4N-Pt_1 (1.21 eV), IrFe-4N-Ir_1 (0.07 eV), and RuFe-4N-Ru_1 (-0.48 eV) on MSAC-4 show more favourable HER activity (closer to zero) due to the co-doped Fe on side, compared to their independent status of Pt_1-4N (1.57 eV), Ir_1-4N (-0.33 eV), and Ru_1-4N (-0.49 eV). In turn, PtFe-4N-Fe_1 (-0.12 eV) and IrFe-4N-Fe_1 (0.08 eV) exhibit better HER activity than Fe_1-4N (0.35 eV), indicating that the synergistic effects from Pt_1, and Ir_1 increase the HER capability of the neighbour Fe single atom. However, RuFe-4N-Fe_1 (0.45 eV) have a minor fade. Our hypothesis is speculated by assuming that all these active sites have an average ratio. The actual ratios of individual dual active sites, however, are challenging to quantitate. The synergistic effects between variable elements on MSAC, thus, are supposed to change their intrinsic electronic structure as well as the catalytic ability.

In summary, based on an anion doped polymer, a versatile tactic is explored to flexibly tune the complexity of carbon surface from mono- to multi-metallic single atom doping. As a result, several active sites can coexist on carbon support, enriching the structural complexity and catalytic chemistry of SACs. In particular, MSAC-6 illustrates an ultrahigh mass activity for ORR compared to the results reported previously. We demonstrates that the atomic-level cooperative interactions in multimetallic SACs directly determine the overall material properties as well as catalytic activity. Also, we concludes that an appropriate combination of compositions on carbon surface can maximize the catalytic efficiency. Our results extend the boundary of SACs and thus, open a new avenue to a range of catalysts in terms of the atomic control of surface complexity and subsequent enhancement of catalytic activity. The high complexity and disordered structure of carbon surface derived from multi-single-atom doping, however, is very complicated and challenging, extraordinary efforts should be devoted to unveil their underlying mechanism on catalytic reactions.

Methods and materials

Materials

Sodium p-toluenesulfonate ($CH_3C_6H_4SO_3Na$, 97%, P-TSNa), Vanadium(III) chloride (VCl_3, 97%), Manganese sulfate monohydrate ($MnSO_4 \cdot H_2O$, 99%), Silver nitrate ($AgNO_3$, 99%), Germanium(II) chloride ($GeCl_2$, 99%), Tungsten(IV) chloride (WCl_4, 95%), Tin(II) chloride ($SnCl_2$, 98%), Rhodium(III) acetylacetonate ($C_{15}H_{21}O_6Rh$, 97%), Cobalt(III) acetylacetonate ($C_{15}H_{21}O_6Co$), Platinum(II) acetylacetonate ($C_{10}H_{14}O_4Pt$, 99%), Iridium(II) acetylacetonate ($C_{10}H_{14}O_4Ir$, 99%), Palladium(II) acetylacetonate ($C_{10}H_{14}O_4Pd$, 99%), Lead(II) chloride ($PbCl_2$, 98%), Bismuth(III) nitrate pentahydrate ($Bi(NO_3)_3 \cdot 5H_2O$, 97%), Ruthenium (III) acetylacetonate ($C_{15}H_{21}O_6Ru$, 97%), Iron (III) acetylacetonate ($C_{15}H_{21}O_6Fe$, 99%), Nickel (II) acetylacetonate ($C_{10}H_{14}O_4Ni$, 99%), Molybdenum(V) isopropoxide ($C_{15}H_{35}MoO_5$, 99%), Copper sulfate ($CuSO_4$, 99%), Indium(III) chloride ($InCl_3$, 98%), Nafion@117 solution (5 wt %, dispersed in a binary solvent of water and lower aliphatic alcohols), commercial Pt black (20 wt. % Pt loading on Vulcan XC72). All the chemical reagents were used as received without any further purification.

Synthesis of S-PPy

In a typical synthesis, S-PPy was prepared by oxidation polymerization reaction. The oxidant ammonia persulfate (1.13 g) was dissolved in 20 ml H_2O, and added slowly under stirring into 200 mL 1M hydrochloride acid containing 0.33 g pyrrole monomer and 0.25 g P-TSNa. The polymerization was carried out at 0–5 ˚C for 24 h. The precipitate was washed for several times with deionized water till the filtrate became neutral, and further washed with ethanol and acetone for several times. The resulting powder was dried overnight at 80 ˚C in a vacuum oven. The compared PPy were prepared in the similar way with S-PPy but without P-TSNa.

Synthesis of MSAC.

In a typical synthesis, 50 mg S-PPy powders were mixed with 50 ml ethanol by ultra-sonification for 30 min to form a homogeneous dispersion. A mixture of metal salts ($C_{10}H_{14}O_4Pt$ (0.0015 mmol), $C_{15}H_{21}O_6Co$ (0.003 mmol), $C_{10}H_{14}O_4Pd$ (0.0015 mmol), $C_{10}H_{14}O_4Ir$ (0.0015 mmol), $C_{15}H_{21}O_6Fe$ (0.003 mmol), $InCl_3$ (0.0010 mmol), $C_{15}H_{21}O_6Ru$ (0.0015 mmol)) were then added into the dispersion, with rigorously stirring until the ethanol evaporated out, forming S-PPy-$M_{mixture}^{x+}$ mixtures. Finally, the mixtures were annealed at 750 °C under argon for 2 h. These resultant products were denoted as MSAC-7. Similarly, the MSAC-6, MSAC-5, MSAC-4, MSAC-3, and MSAC-2 were prepared in a same way of MSAC-7 by using their corresponding mixture of designable elements, which have a same concentration with the metal salts of MSAC-7.

Synthesis of M_1@NC.

In a typical synthesis, 50 mg PPy powders were mixed with 50 ml ethanol by ultra-sonification for 30 min to form a homogeneous dispersion. 0.0075 mmol metal salts were then added into the dispersion, with rigorously stirring until the ethanol evaporated out, forming S-PPy-M^{x+} mixtures, respectively. Finally, the mixtures were annealed at 750 °C under argon for 2 h. These resultant products were denoted as M_1@NC, respectively.

Characterization.

High-angle annular dark-field - scanning transmission electron microscope (HAADF-STEM) images, EELS image and STEM energy dispersive X-ray spectroscopy (STEM-EDS) data were acquired on a transmission electron microscopy system (TEM, JEOL ARM-200F, 200 kV). The XRD patterns were collected by powder X-ray diffraction (XRD; GBC MMA diffractometer) with Cu Kα radiation at a scan rate of 3 ° min^{-1}. The bonding on Pt_1@Co/CN was determined by X-ray photoelectron spectroscopy (XPS; PHOIBOS 100 Analyser from SPECS, Berlin, Germany; Al Kα X-rays). The loading mass was determined by inductively coupled plasma – optical emission

spectrometry (ICP-AES, IRIS Intrepid ER/S, Thermo Elemental). Fourier transform infrared spectroscopy (FTIR) was performed at room temperature on a Shimadzu Prestige-21. Raman spectroscopy was used to determine the length of bonds on a Jobin Yvon HR800. X-ray absorption spectroscopy (XAS) experiments were carried out at the applied X-ray absorption fine structure spectroscopy (XAFS) at Japan Synchrotron Radiation Research Institute (JASRI) (1-1-1, Kouto, Sayo-cho, Sayo-gun, Hyogo 679-5198 Japan).

Electrochemical Measurements.

Before the glassy carbon electrode (GCE) was used for rotating disk electrode (RDE) measurements, it was consecutively polished with 1.0 and 0.05 μm alumina powder, rinsed with deionized water, and sonicated first in ethanol and then in water. Typically, working electrodes were prepared by mixing the catalyst with deionized water + isopropanol + 5% Nafion® (v/v/v = 4/1/0.05). The loading mass on the rotating disk electrode (RDE) was calculated as 100.2 μg cm^{-2}. A graphite electrode was used as the counter electrode, and Ag/AgCl (KCl, 3M) was used as the reference electrode, with all potentials referred to reversible hydrogen electrode (RHE). Thus, the potential with respect to RHE can be calculated as follows: E(RHE) = E(Ag/AgCl) + 0.059 × pH + 0.210. Before testing, flowing N_2 was bubbled through the electrolyte in the cell to achieve an N_2-saturated solution. The ORR tests were carried out in 0.1 M KOH by using a computer-controlled potentiostat (Princeton 2273 and 616, Princeton Applied Research) in a conventional three-electrode cell at room temperature. Before testing, flowing N_2/O_2 was bubbled through the electrolyte in the cell to achieve an N_2/O_2-saturated solution. The oxygen reduction reaction (ORR) testing was carried out in O_2-saturated 0.1 M KOH solution at different rotation rates with a scan rate of 10 mV s^{-1}. Accelerated durability tests were performed at room temperature in O_2-saturated 0.1 M KOH solution by applying cyclic potential sweeps between 0.6 and 1.0 V versus RHE at a scan rate of 50 mV s^{-1} for 10000 cycles. The kinetic current (I_k) can be calculated using the Koutecky-Levich (K-L) equation, which is expressed by

$$\frac{1}{I} = \frac{1}{I_k} + \frac{1}{I_d}$$

where I is the measured current and I_d the diffusion limited current.

The K-L plot is based on the Levich equation:

$$I_d = 0.62nFAD^{2/3}\upsilon^{-1/6}\omega^{1/2}C_{O_2}$$

where n is the number of electrons transferred; F is Faraday's constant; A is the area of the electrode (0.196 cm^2); D is the diffusion coefficient of O_2 in 0.1 M KOH; υ is the kinematic viscosity of the electrolyte; ω is the angular frequency of rotation, $\omega = 2\pi f/60$, where f is the RDE rotation rate in rpm and C_{O_2} is the concentration of molecular oxygen in 0.1 M KOH solution. The HER tests were carried out in N_2-saturated 1 M KOH solution with a scan rate of 10 mV s^{-1}.

Computational details.

All calculations were performed by the spin-polarized density functional theory (DFT) methods as implemented in the Vienna Ab initio Simulation Package (VASP) [33-34]. The Perdew-Burke-Ernzerhof (PBE) exchange-correlation functional within a generalized gradient approximation (GGA) was employed, and a 400 eV cutoff energy for the plane-wave basis set was used for the valence electrons. The convergence threshold was 10^{-5} eV for energy and 0.02 eV/Å for force, respectively.

To simulate a defective graphene monolayer, a periodic 4 × 4 supercell was built. To avoid the interactions between two adjacent periodic images, the vacuum thickness was set to be 20 Å. The Brillouin zone was sampled using the 3 × 3 × 1 Monkhorst-Pack k-point mesh in structure

optimization, and the semiempirical dispersion-corrected DFT force-field approach (DFT-D3) [35] was adopted to describe the interaction involved in the calculations.

The ΔG value can be determined as: $\Delta G = \Delta E + \Delta_{ZPE} - T\Delta S + \Delta G_U + \Delta G_{pH}$, where ΔE is the difference in electron energy obtained directly from the DFT calculation, ΔZPE is the change in zero-point energies, T is the temperature (T = 298.15K), and ΔS is the entropy change. ΔG_U is the free energy contribution related to electrode potential U. ΔG_{pH} is the correction of the H^+ free energy by the concentration, which can be determined as $\Delta G_{pH} = 2.303 \times k_B T \times pH$ (or $0.059 \times pH$), where k_B is the Boltzmann constant.

For ORR, The change in Gibbs free energy (ΔG) of the various intermediates was expressed as:

$$\Delta G = \Delta E + \Delta \mathrm{ZPE} - T\Delta S$$

where ΔE is the reaction energy of the elementary steps, ΔZPE is the zero point energy change, T is the temperature at 298.15 K, and ΔS is the entropy change. ΔZPE and ΔS could be obtained from calculations of the vibrational frequency of intermediates and gas phase species, which were obtained from the NIST database. H_2O and H_2 can be well described within the framework of DFT calculations. The entropy of gas-phase water was calculated to be 0.035 bar which is due to the equilibrium pressure at room temperature. The free energy change is fixed at the experimental value of 2.46 eV for the total reaction: $H_2O \rightarrow 1/2O_2 + H_2$. So, the free energy of O_2 can be obtained from $G(\mathrm{O_2}) = 4.92 + 2(G(\mathrm{H_2O}) - G(\mathrm{H_2}))$.

References

1. Fei, H.; Dong, J.; Feng, Y.; Allen, C. S.; Wan, C.; Volosskiy, B.; Li, M.; Zhao, Z.; Wang, Y.; Sun, H., General synthesis and definitive structural identification of MN 4 C 4 single-atom catalysts with tunable electrocatalytic activities. *Nature Catalysis* **2018,** *1* (1), 63.
2. Lai, W. H.; Miao, Z.; Wang, Y. X.; Wang, J. Z.; Chou, S. L., Atomic-Local Environments of Single-Atom Catalysts: Synthesis, Electronic Structure, and Activity. *Advanced Energy Materials* **2019**.
3. Gong, K.; Du, F.; Xia, Z.; Durstock, M.; Dai, L., Nitrogen-doped carbon nanotube arrays with high electrocatalytic activity for oxygen reduction. *science* **2009,** *323* (5915), 760-764.
4. Kim, D.-w.; Li, O. L.; Saito, N., Enhancement of ORR catalytic activity by multiple heteroatom-doped carbon materials. *Physical Chemistry Chemical Physics* **2015,** *17* (1), 407-413.
5. Daelman, N.; Capdevila-Cortada, M.; López, N., Dynamic charge and oxidation state of Pt/CeO2 single-atom catalysts. *Nature materials* **2019**.
6. Jones, J.; Xiong, H.; DeLaRiva, A. T.; Peterson, E. J.; Pham, H.; Challa, S. R.; Qi, G.; Oh, S.; Wiebenga, M. H.; Hernández, X. I. P., Thermally stable single-atom platinum-on-ceria catalysts via atom trapping. *Science* **2016,** *353* (6295), 150-154.
7. Wei, H.; Liu, X.; Wang, A.; Zhang, L.; Qiao, B.; Yang, X.; Huang, Y.; Miao, S.; Liu, J.; Zhang, T., FeO x-supported platinum single-atom and pseudo-single-atom catalysts for chemoselective hydrogenation of functionalized nitroarenes. *Nature communications* **2014,** *5*, 5634.
8. Zhang, Z.; Zhu, Y.; Asakura, H.; Zhang, B.; Zhang, J.; Zhou, M.; Han, Y.; Tanaka, T.; Wang, A.; Zhang, T., Thermally stable single atom Pt/m-Al 2 O 3 for selective hydrogenation and CO oxidation. *Nature communications* **2017,** *8*, 16100.
9. Lucci, F. R.; Liu, J.; Marcinkowski, M. D.; Yang, M.; Allard, L. F.; Flytzani-Stephanopoulos, M.; Sykes, E. C. H., Selective hydrogenation of 1, 3-butadiene on platinum–copper alloys at the single-atom limit. *Nature communications* **2015,** *6*, 8550.

10. Cheng, N.; Stambula, S.; Wang, D.; Banis, M. N.; Liu, J.; Riese, A.; Xiao, B.; Li, R.; Sham, T.-K.; Liu, L.-M., Platinum single-atom and cluster catalysis of the hydrogen evolution reaction. *Nature communications* **2016,** *7*, 13638.
11. Ou, M.; Wan, S.; Zhong, Q.; Zhang, S.; Wang, Y., Single Pt atoms deposition on g-C3N4 nanosheets for photocatalytic H2 evolution or NO oxidation under visible light. *International Journal of Hydrogen Energy* **2017,** *42* (44), 27043-27054.
12. Yin, P.; Yao, T.; Wu, Y.; Zheng, L.; Lin, Y.; Liu, W.; Ju, H.; Zhu, J.; Hong, X.; Deng, Z., Single cobalt atoms with precise N-coordination as superior oxygen reduction reaction catalysts. *Angewandte chemie international edition* **2016,** *55* (36), 10800-10805.
13. Chen, P.; Zhou, T.; Xing, L.; Xu, K.; Tong, Y.; Xie, H.; Zhang, L.; Yan, W.; Chu, W.; Wu, C., Atomically dispersed iron–nitrogen species as electrocatalysts for bifunctional oxygen evolution and reduction reactions. *Angewandte Chemie International Edition* **2017,** *56* (2), 610-614.
14. Qiao, B.; Wang, A.; Yang, X.; Allard, L. F.; Jiang, Z.; Cui, Y.; Liu, J.; Li, J.; Zhang, T., Single-atom catalysis of CO oxidation using Pt 1/FeO x. *Nature chemistry* **2011,** *3* (8), 634.
15. Gao, G.; Jiao, Y.; Waclawik, E. R.; Du, A., Single atom (Pd/Pt) supported on graphitic carbon nitride as an efficient photocatalyst for visible-light reduction of carbon dioxide. *Journal of the American Chemical Society* **2016,** *138* (19), 6292-6297.
16. Tao, H.; Choi, C.; Ding, L.-X.; Jiang, Z.; Han, Z.; Jia, M.; Fan, Q.; Gao, Y.; Wang, H.; Robertson, A. W., Nitrogen fixation by Ru single-atom electrocatalytic reduction. *Chem* **2019,** *5* (1), 204-214.
17. Zang, W.; Sumboja, A.; Ma, Y.; Zhang, H.; Wu, Y.; Wu, S.; Wu, H.; Liu, Z.; Guan, C.; Wang, J., Single Co Atoms Anchored in Porous N-Doped Carbon for Efficient Zinc− Air Battery Cathodes. *ACS Catalysis* **2018,** *8* (10), 8961-8969.
18. Du, Z.; Chen, X.; Hu, W.; Chuang, C.; Xie, S.; Hu, A.; Yan, W.; Kong, X.; Wu, X.; Ji, H., Cobalt in Nitrogen-Doped Graphene as Single-Atom Catalyst for High-Sulfur Content Lithium–Sulfur Batteries. *Journal of the American Chemical Society* **2019,** *141* (9), 3977-3985.
19. Zhang, B.-W.; Sheng, T.; Liu, Y.-D.; Wang, Y.-X.; Zhang, L.; Lai, W.-H.; Wang, L.; Yang, J.; Gu, Q.-F.; Chou, S.-L., Atomic cobalt as an efficient electrocatalyst in sulfur cathodes for superior room-temperature sodium-sulfur batteries. *Nature communications* **2018,** *9* (1), 4082.
20. Guo, X.; Fang, G.; Li, G.; Ma, H.; Fan, H.; Yu, L.; Ma, C.; Wu, X.; Deng, D.; Wei, M., Direct, nonoxidative conversion of methane to ethylene, aromatics, and hydrogen. *Science* **2014,** *344* (6184), 616-619.
21. Lin, L.; Zhou, W.; Gao, R.; Yao, S.; Zhang, X.; Xu, W.; Zheng, S.; Jiang, Z.; Yu, Q.; Li, Y.-W., Low-temperature hydrogen production from water and methanol using Pt/α-MoC catalysts. *Nature* **2017,** *544* (7648), 80.
22. Wang, A.; Li, J.; Zhang, T., Heterogeneous single-atom catalysis. *Nature Reviews Chemistry* **2018,** *2* (6), 65.
23. Lee, B.-H.; Park, S.; Kim, M.; Sinha, A. K.; Lee, S. C.; Jung, E.; Chang, W. J.; Lee, K.-S.; Kim, J. H.; Cho, S.-P., Reversible and cooperative photoactivation of single-atom Cu/TiO 2 photocatalysts. *Nature materials* **2019,** *18* (6), 620.
24. Chen, M.; Goodman, D., The structure of catalytically active gold on titania. *science* **2004,** *306* (5694), 252-255.
25. Sun, S.; Zhang, G.; Gauquelin, N.; Chen, N.; Zhou, J.; Yang, S.; Chen, W.; Meng, X.; Geng, D.; Banis, M. N., Single-atom catalysis using Pt/graphene achieved through atomic layer deposition. *Scientific reports* **2013,** *3*, 1775.

26. He, X.; He, Q.; Deng, Y.; Peng, M.; Chen, H.; Zhang, Y.; Yao, S.; Zhang, M.; Xiao, D.; Ma, D., A versatile route to fabricate single atom catalysts with high chemoselectivity and regioselectivity in hydrogenation. *Nature communications* **2019,** *10* (1), 1-9.
27. Yang, H.; Shang, L.; Zhang, Q.; Shi, R.; Waterhouse, G. I.; Gu, L.; Zhang, T., A universal ligand mediated method for large scale synthesis of transition metal single atom catalysts. *Nature Communications* **2019,** *10* (1), 1-9.
28. Zhang, L.; Fischer, J. M. T. A.; Jia, Y.; Yan, X.; Xu, W.; Wang, X.; Chen, J.; Yang, D.; Liu, H.; Zhuang, L.; Hankel, M.; Searles, D. J.; Huang, K.; Feng, S.; Brown, C. L.; Yao, X., Coordination of Atomic Co–Pt Coupling Species at Carbon Defects as Active Sites for Oxygen Reduction Reaction. *Journal of the American Chemical Society* **2018,** *140* (34), 10757-10763.
29. Liu, R.; Iddir, H.; Fan, Q.; Hou, G.; Bo, A.; Ley, K. L.; Smotkin, E.; Sung, Y.-E.; Kim, H.; Thomas, S., Potential-dependent infrared absorption spectroscopy of adsorbed CO and X-ray photoelectron spectroscopy of arc-melted single-phase Pt, PtRu, PtOs, PtRuOs, and Ru electrodes. *The Journal of Physical Chemistry B* **2000,** *104* (15), 3518-3531.
30. Teliska, M.; O'Grady, W.; Ramaker, D., Determination of H adsorption sites on Pt/C electrodes in HClO4 from Pt L23 X-ray absorption spectroscopy. *The Journal of Physical Chemistry B* **2004,** *108* (7), 2333-2344.
31. Nørskov, J. K.; Rossmeisl, J.; Logadottir, A.; Lindqvist, L.; Kitchin, J. R.; Bligaard, T.; Jonsson, H., Origin of the overpotential for oxygen reduction at a fuel-cell cathode. *The Journal of Physical Chemistry B* **2004,** *108* (46), 17886-17892.
32. Jiao, Y.; Zheng, Y.; Davey, K.; Qiao, S.-Z., Activity origin and catalyst design principles for electrocatalytic hydrogen evolution on heteroatom-doped graphene. *Nature Energy* **2016,** *1*, 16130.
33. Kresse, G.; Furthmüller, J., Efficient iterative schemes for ab initio total-energy calculations using a plane-wave basis set. *Physical review B* **1996,** *54* (16), 11169.
34. Kresse, G.; Joubert, D., From ultrasoft pseudopotentials to the projector augmented-wave method. *Physical Review B* **1999,** *59* (3), 1758.
35. Grimme, S., Semiempirical GGA-type density functional constructed with a long-range dispersion correction. *Journal of computational chemistry* **2006,** *27* (15), 1787-1799.

Acknowledgments
This work is financially supported by the Australian Research Council (ARC) (DE170100928), and Australian Renewable Energy Agency (ARENA) Project (G00849). We thank the UOW Electron Microscopy Centre for use of the facilities (LE0882813 and LE0237478) and Dr. Tania Silver for critical reading of the manuscript. We also thank Lin Li, Li Wang, and Min Liu for their help in characterization. The synchrotron radiation experiments were performed at Japan Atomic Energy Agency (JAEA) beamline BL14B1 in SPring-8 (Proposal Nos. 2018A3634 and 2018B3634) under the Shared Use Program of JAEA Facilities (Proposal Nos. 2018A-E01 and 2018B-E01) with the approval of the Nanotechnology Platform project supported by the Ministry of Education, Culture, Sports, Science and Technology (Proposal Nos. A-18-AE-0001 and A-18-AE-0023).

Author contributions
W.H.L., Y.-X. W., L. W., S.- L. C. designed the experiments. W.-H. L. and W.Z. synthesized the samples. H. W., H. Y., L.F.Z. and D. M. performed XAS experiments and analysed the results. H.W.L., Y.J.L., and Z.C.Y. done FTRI and Raman characterization. Q. J. and Q. S. performed the

ab initio calculations. The project was planned, directed and supervised by J.Z.W., H.-K. L., S.-L. C. L. W., and S.-X. D. All authors discussed the results and contributed to manuscript preparation.

Competing interests
The authors declare no competing interests.

Additional information
Supplementary information:

Supplementary Figs. S1-26, Tables 1-3